

# The Serpens filament: at the onset of slightly supercritical collapse

Y. Gong<sup>1,2</sup>, G. X. Li<sup>3,4</sup>, R. Q. Mao<sup>2</sup>, C. Henkel<sup>1,5,6</sup>, K. M. Menten<sup>1</sup>, M. Fang<sup>7</sup>, M. Wang<sup>2</sup> and J. X. Sun<sup>2</sup>

天体：Serpens filament (最も近いIRDCsの一つ; d ~440pc)

望遠鏡：Purple Mountain Observatory 13.7 m望遠鏡

輝線：C<sup>18</sup>O, HCO<sup>+</sup>, HNC, HCN, N<sub>2</sub>H<sup>+</sup>, CS, CH<sub>3</sub>OH

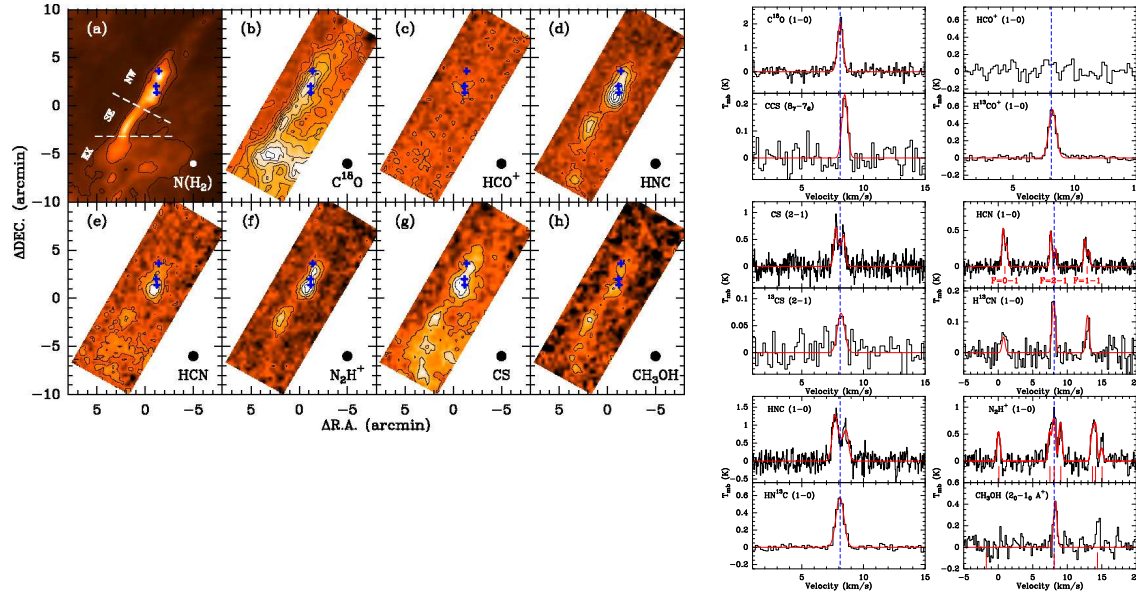


**Table 1.** Observed parameters of the molecular lines used in the work.

Line	Frequency (GHz)	$E_u/k$ (K)	$B_{ul}$ (K)	$\Delta v$ (km s <sup>-1</sup> )	$\Delta v$ (kHz)	$\sigma$ (K)	obs.Mode
(1)	(2)	(3)	(4)	(5)	(6)	(7)	(8)
The Serpens filament							
C <sup>18</sup> O (1-0)	109.78217	5.0	55.5%	0.04	12.2	0.27	mapping
HCO <sup>+</sup> (1-0)	89.18852	4.3	56.8%	0.21	61	0.07	mapping
HCN (1-0)	88.63185	4.3	56.8%	0.21	61	0.07	mapping
N <sub>2</sub> H <sup>+</sup> (1-0)	93.173.76	4.5	61.9%	0.04	12.2	0.20	mapping
CS (2-1)	97.98095	7.1	60.6%	0.04	12.2	0.13	mapping
HNC (1-0)	90.66357	4.4	57.0%	0.04	12.2	0.16	mapping
CH <sub>3</sub> OH ( $J_K=2_0-1_0$ A <sup>+</sup> )	96.74138	7.0	63.4%	0.19	61	0.07	mapping
CH <sub>3</sub> OH ( $J_K=2_0-1_0$ E)	96.73936	12.5	63.4%	0.19	61	0.07	mapping
Source A: ( $\alpha_{J2000}=18^{\circ}28'47.62$ , $\delta_{J2000}=00^{\circ}50'55.7$ )							
HCN (1-0)	88.63185	4.3	56.8%	0.04	12.2	0.06	pointing
H <sup>13</sup> CO <sup>+</sup> (1-0)	86.75429	4.2	56.7%	0.21	61	0.02	pointing
H <sup>13</sup> CN (1-0)	86.34018	4.1	56.7%	0.21	61	0.02	pointing
HN <sup>13</sup> C (1-0)	87.09085	4.2	56.7%	0.21	61	0.02	pointing
<sup>13</sup> CS (2-1)	92.49426	6.7	61.9%	0.20	61	0.02	pointing
CCS ( $J_K=8_0-7_0$ )	93.87011	19.9	61.9%	0.19	61	0.04	pointing
Source B: ( $\alpha_{J2000}=18^{\circ}28'57.70$ , $\delta_{J2000}=00^{\circ}48'02.0$ )							
HCN (1-0)	88.63185	4.3	56.8%	0.04	12.2	0.06	pointing

HCO<sup>+</sup>, HNC, HCN, CS：自己吸収が見られる

C<sup>18</sup>O：フィラメント構造をよく示す。

velocity coherentな音速フィラメント。

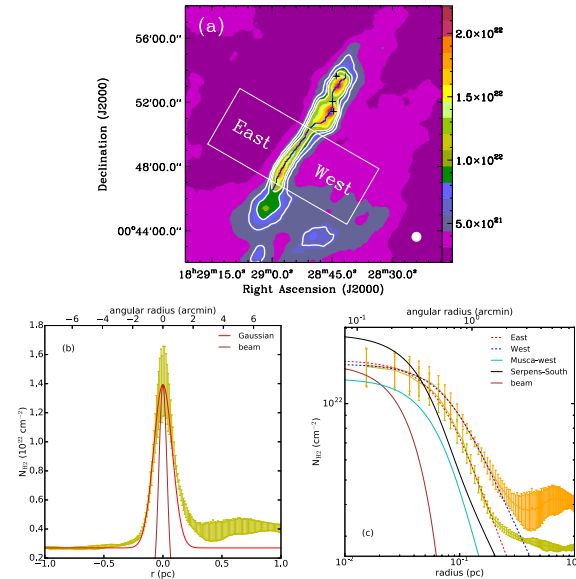


**Fig. 10.** (a) The H<sub>2</sub> column density image of the Serpens filament obtained from the Herschel Gould belt survey. The contours correspond to column densities of  $6 \times 10^{21}$  cm<sup>-2</sup>,  $8 \times 10^{21}$  cm<sup>-2</sup>, and  $1 \times 10^{22}$  cm<sup>-2</sup>. The extracted crest of the Serpens filament is marked with the blue line. The emission within the white box is used to derive the radial profile of H<sub>2</sub> column density. The three black crosses give the positions of the three embedded YSOs. The offsets increase from east to west. (b) The mean radial profile of H<sub>2</sub> column densities within the white box in Fig. 10a. The offsets increase from east to west. A Gaussian fit is indicated by the red line. (c) The mean radial H<sub>2</sub> column density profile on the west (yellow) and east (orange) sides of the crest. The red and blue dashed lines represent Plummer-like fits to the east and west (see Fig. 10a) within a radius range of <0.2 pc, while the cyan and black lines represent the beam-convolved radial profile of Musca-West (Kainulainen et al. 2016) and the Serpens South filament (Kirk et al. 2013). In both Figs. 10a and 10b. The beam size is shown by the brown line.

Filament crestに沿ったCD profile :  $\sim 0.85$  pcと $\sim 0.26$  pcのfragmentation scaleを示す

$\sim 0.85$  pc : Filamentのfragmentation scale

$\sim 0.26$  pc : thermal Jeans instability or YSOからのfeedback ?

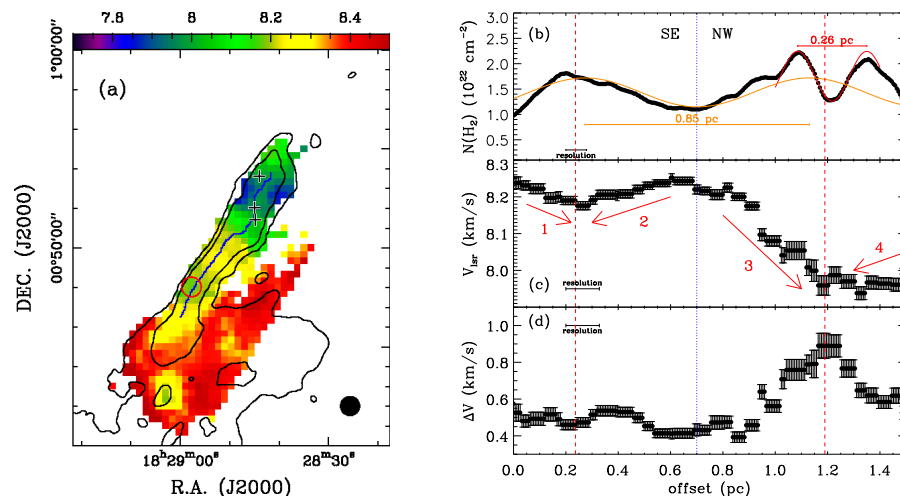


**Fig. 11.** (a) The LSR velocity map similar to Fig. 4b but overlaid with the  $\text{H}_2$  column density contours which represent  $4 \times 10^{21} \text{ cm}^{-2}$  and  $6 \times 10^{21} \text{ cm}^{-2}$ . Source B is marked with the red circle, and the three black crosses give the positions of the three embedded YSOs, i.e., em10, em28, and em16. (b) The column density profile along the crest of the Serpens filament indicated by the blue line in Fig. 11a. The spatial resolution is  $\sim 0.08$  pc. The offset increases from south to north. The red line represents a sinusoidal fit to the profile within the offset range of 1.0–1.4 pc. A sinusoidal orange line is created to better visualize the variation at a large scale. (c) Similar to Fig. 11b but for the  $\text{C}^{18}\text{O}$  (1–0) velocity. The four red arrows correspond to the velocity gradients in Fig. 4b, indicated there by black arrows. (d) Similar to Fig. 11c but for the  $\text{C}^{18}\text{O}$  (1–0) line widths. In Figs. 11b–11d, the red dashed lines mark the positions of Source B and the YSO emb28.

Serpens filamentはわずかにSupercritical (Line mass  $\sim 36\text{--}41 M_{\text{sun}} \text{ pc}^{-1}$ )

blue-skewed HNC · CNと、HCNのhyperfine : (tras-)sonic filamentでのradial collapseを示唆？

「わずかにSupercriticalなfilamentは、collapseする傾向にある」という理論とも合う

HCNとCSのblue-skewed profileから、

- radial infall vel. はfree-fall vel. の10%以下
- radila collapseのinfall rateは  $\sim 72 \text{ M}_{\text{sun}} \text{ Myr}^{-1}$   
 $\Rightarrow$  filamentの質量を2倍にするには $\sim 0.9 \text{ Myr}$ 必要

Class I天体を作る時間と同等

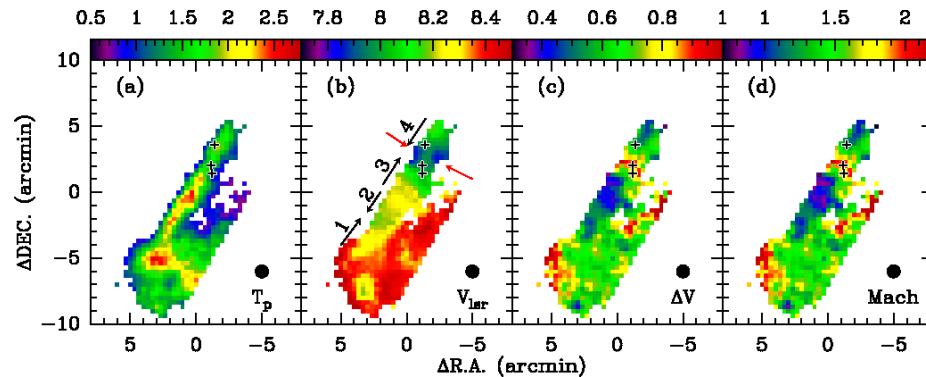


Fig. 4. Maps of peak intensities (Fig. 4a), LSR velocities (Fig. 4b), line widths (Fig. 4c), and Mach numbers (Fig. 4d) derived from single-component Gaussian fits to our  $\text{C}^{18}\text{O}$  (1–0) data. The color bars represent main beam brightness temperatures in units of K in Fig. 4a, LSR velocities in units of  $\text{km s}^{-1}$  in Fig. 4b, and line widths in units of  $\text{km s}^{-1}$  in Fig. 4c. Velocity gradients along the filament and perpendicular to the filament are indicated by the black and red arrows in Fig. 4b, respectively. In all panels, the (0, 0) offset corresponds to  $\alpha_{\text{J2000}} = 18^{\text{h}}28^{\text{m}}49^{\text{s}}.642$ ,  $\delta_{\text{J2000}} = 00^{\circ}50'01''.08$ , and the three black crosses give the positions of the three embedded YSOs (see Fig. 1). The mean uncertainties in derived peak intensities, LSR velocities, line widths, and Mach numbers are 0.19 K, 0.02  $\text{km s}^{-1}$ , 0.06  $\text{km s}^{-1}$ , and 0.1, respectively. The beam size is shown in the lower right of each panel.

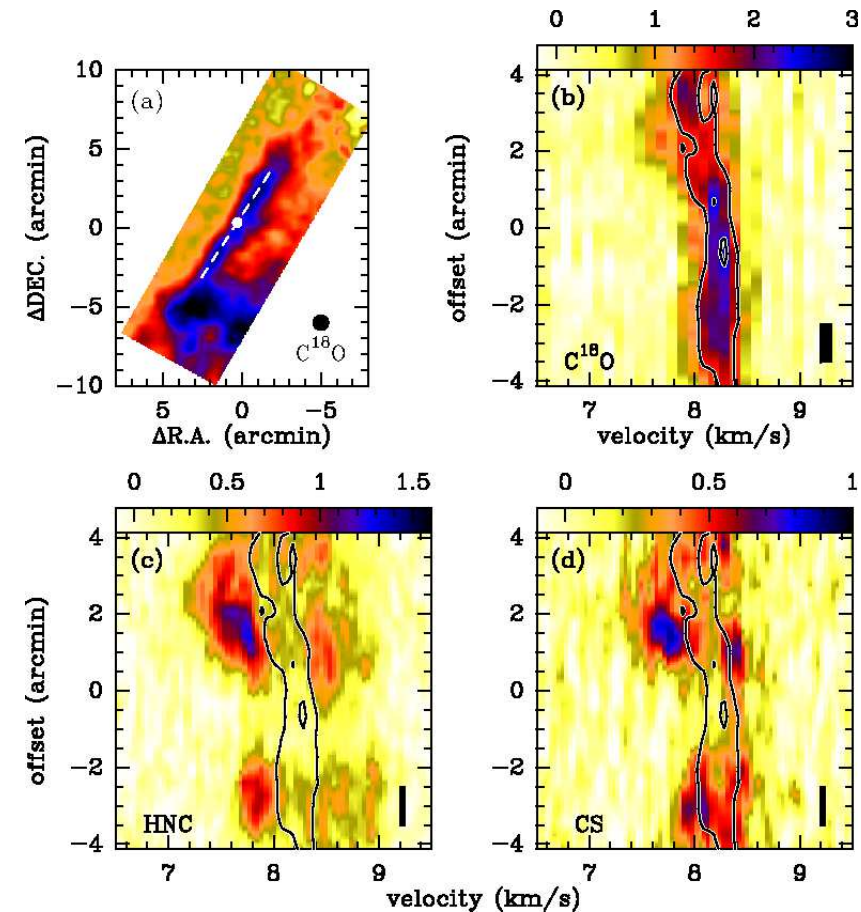


Fig. 9. (a) The  $\text{C}^{18}\text{O}$  (1–0) integrated intensity map similar to Fig. 2b but overlaid with a PV cut indicated by the white dashed line. (b) The PV diagram of  $\text{C}^{18}\text{O}$  (1–0) along the PV cut in Fig. 9a. The channel width of  $\text{C}^{18}\text{O}$  (1–0) spectra has been binned to 0.1  $\text{km s}^{-1}$  to achieve a higher dynamical range. (c) Similar to Fig. 9b but for HNC (1–0). (d) Similar to Fig. 9b but for CS (2–1). In Fig. 9b–d, the color bars represent main beam brightness temperatures in units of K, and the black contours represent the  $\text{C}^{18}\text{O}$  (1–0) emission starting at 1.5 K ( $5\sigma$ ) with increments of 0.9 K ( $3\sigma$ ). The offsets are given with respect to the center of the PV cut ( $\alpha_{\text{J2000}} = 18^{\text{h}}28^{\text{m}}50^{\text{s}}.865$ ,  $\delta_{\text{J2000}} = 00^{\circ}50'21''.799$ , also indicated by the white filled circle in Fig. 9a), and increase from southeast to northwest. The resolution element is shown in the lower right of each panel.

Filamentの長軸に沿った $\text{C}^{18}\text{O}$ の速度勾配：Filament内のGas accretionを示唆 ( $\sim 10 \text{ M}_{\text{sun}} \text{ Myr}^{-1}$ )

速度や密度構造から、このaccretion flowは、Filament長軸方向のcollapseが原因

Infall rateもFilamentに沿ったaccretion rateも、他の報告されているFilamentのものよりも低い

collapseが始まったばかりの初期ステージにある or 熱的&非熱的支えが効果的であることを示す



# CO observations toward the isolated mid-infrared bubble GAL 334.53+00.83 (S44): External triggering of O-star formation by a cloud-cloud collision

Mikito Kohno<sup>1</sup>, Kengo Tachihara<sup>1</sup>, Shinji Fujita<sup>1</sup>, Yusuke Hattori<sup>1</sup>, Kazufumi Torii<sup>2</sup>, Atsushi Nishimura<sup>1</sup>, Misaki Hanaoka<sup>1</sup>, Satoshi Yoshiike<sup>1</sup>, Rei Enokiya<sup>1</sup>, Keisuke Hasegawa<sup>1</sup>, Akio Ohama<sup>1</sup>, Hidetoshi Sano<sup>1,3</sup>, Hiroaki Yamamoto<sup>1</sup> and Yasuo Fukui<sup>1,3</sup>

天体：中間赤外bubble S44  
望遠鏡：NANTEN2, Mopra, ASTE

Telescope	Line	HPBW	Velocity Resolution	RMS noise <sup>(2)</sup> level
NANTEN2	<sup>12</sup> CO $J=1-0$	160''	0.16 km s <sup>-1</sup>	~ 1.2 K
Mopra	<sup>12</sup> CO $J=1-0$	33±2'' <sup>(1)</sup>	0.088 km s <sup>-1</sup>	~ 0.76 K
	<sup>13</sup> CO $J=1-0$	33±2'' <sup>(1)</sup>	0.092 km s <sup>-1</sup>	~ 0.53 K
ASTE	<sup>12</sup> CO $J=3-2$	22''	0.11 km s <sup>-1</sup>	~ 0.3 K

Telescope/Survey	Band	Resolution	References
Spitzer/GLIMPSE	3.6 $\mu$ m	~2''	[1,2]
Spitzer/GLIMPSE	8.0 $\mu$ m	~2''	[1,2]
Spitzer/MIPSGAL	24 $\mu$ m	6''	[3]
APEX/ATLASGAL	870 $\mu$ m	19''	[4]
MOST/SUMSS	843 MHz	~60''	[5]

<sup>1</sup> Reference : Ladd et al. (2005).

<sup>2</sup> The values of the rms noise levels after smoothing the (space and/or velocity) data sets.

References [1] Benjamin et al. (2003), [2] Churchwell et al. (2009), [3] Carey et al. (2009), [4] Schuller et al. (2009), [5] Bock et al. (1999)

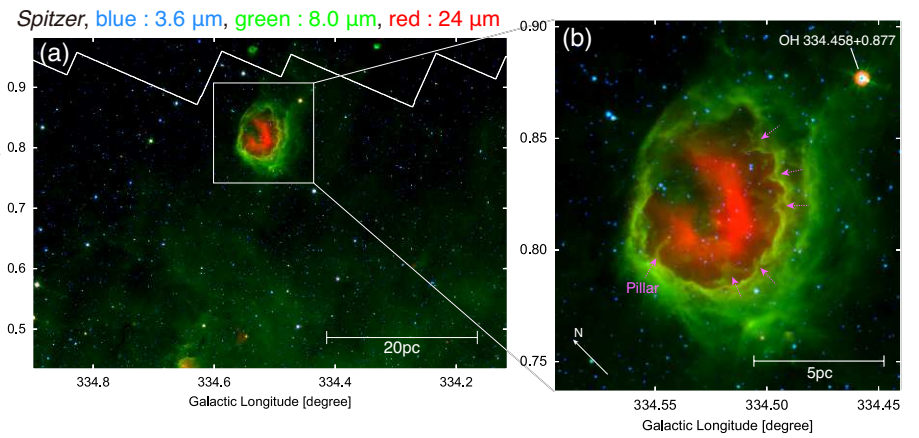


Fig. 1. (a) Large-scale three-color composite images of S44. Blue, green, and red show the *Spitzer*/IRAC 3.6- $\mu$ m, *Spitzer*/IRAC 8- $\mu$ m, and *Spitzer*/MIPS 24- $\mu$ m results. The jagged white line along the Galactic latitude at  $b \sim 0^\circ 95$  shows the observing limit of *Spitzer*/MIPS 24- $\mu$ m. (b) A close-up image of (a). The colors are the same as in (a). The pink dotted arrows indicate the pillar-like structures.

Bubbleの方向に、-84 km s<sup>-1</sup>と-79 km s<sup>-1</sup>の二つ分子雲を同定

-84 km s<sup>-1</sup>の分子雲：Bubbleの外側まで広く分布、南側ではR<sub>3-2/1-0</sub>は0.6以上

-79 km s<sup>-1</sup>の分子雲：8  $\mu$ mの放射と形状が一致、R<sub>3-2/1-0</sub>は0.8以上

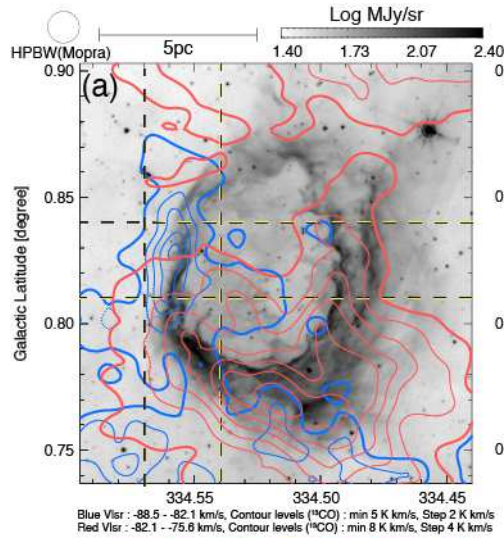


Fig. 6. (a) Integrated intensity map of <sup>13</sup>CO  $J=1-0$  obtained by Mopra for the -84 km s<sup>-1</sup> cloud (blue contours) and the -79 km s<sup>-1</sup> cloud (red contours) superposed on the *Spitzer* 8 $\mu$ m emission. The yellow dashed lines show the integration ranges in latitude and longitude. (b) Galactic latitude-velocity diagram integrated over the longitude range from 334.54 to 334.57. The 1 $\sigma$  noise level is ~ 0.004 K degree for the longitude interval of 0.03. (c) Galactic longitude-velocity diagram integrated over the latitude range from 0.81 to 0.84. The dashed lines represent the radio-recombination-line velocity (-77 km s<sup>-1</sup>) from Caswell and Haynes (1987). The spatial and velocity resolution are smoothed to 52'' and 0.18 km s<sup>-1</sup>, respectively. The 1 $\sigma$  noise level is ~ 0.004 K degree for the latitude interval of 0.03.

電離ガス（左） coldダストの画像（右）：Bubbleとの空間的な相関関係を示す

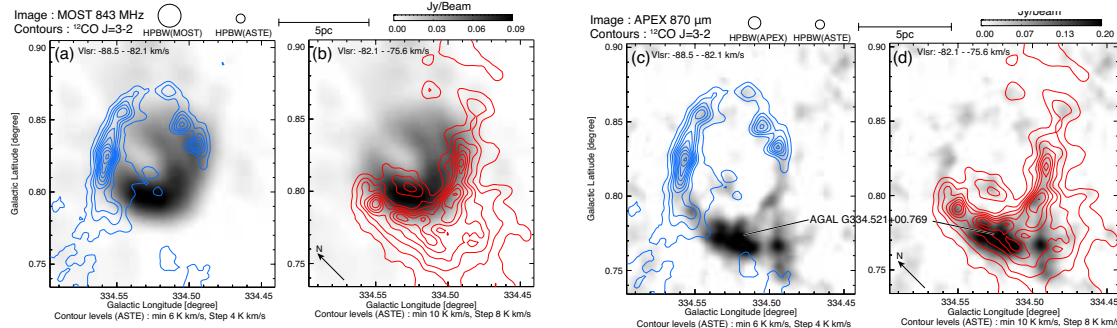


Fig. 9. (a), (b) Integrated intensity map of <sup>12</sup>CO  $J=3-2$  (contours) obtained with ASTE superposed on the MOST 843 MHz continuum image. (c), (d) Integrated intensity map of <sup>12</sup>CO  $J=3-2$  (contours) obtained by ASTE superposed on the APEX 870  $\mu$ m continuum image. The blue and red contours represent the -84 km s<sup>-1</sup> cloud and the -79 km s<sup>-1</sup> cloud, respectively.

励起星をO8.5-9 (~20 M<sub>sun</sub>) と見積もった (from SUMSS 843 MHz (36 cm)、単一星と仮定)

$$\left[ \frac{N_{Ly}}{s^{-1}} \right] \sim 4.761 \times 10^{48} a(\nu, T_e)^{-1} \left[ \frac{\nu}{GHz} \right]^{0.1} \left[ \frac{T_e}{K} \right]^{-0.45} \left[ \frac{S_\nu}{Jy} \right] \left[ \frac{D}{kpc} \right]^2,$$

$$N_{Ly} \sim 10^{48.08} s^{-1}$$

二つの分子雲は、中間の速度で見られるbridge  
で繋がっている (Bubbleの東側)

2つの分子雲の相互作用によるものと解釈される

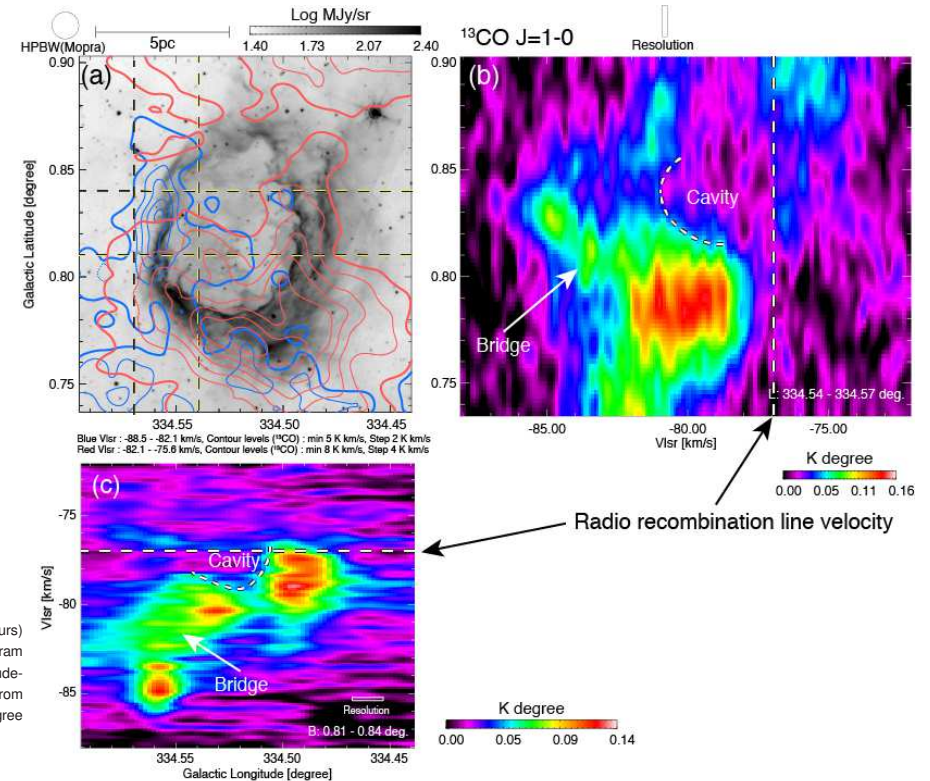


**Fig. 6.** (a) Integrated intensity map of  $^{13}\text{CO } J=1-0$  obtained by Mopra for the  $-84 \text{ km s}^{-1}$  cloud (blue contours) and the  $-79 \text{ km s}^{-1}$  cloud (red contours) superposed on the *Spitzer*  $8\mu\text{m}$  emission. The yellow dashed lines show the integration ranges in latitude and longitude. (b) Galactic latitude-velocity diagram integrated over the longitude range from  $334.54$  to  $334.57$ . The  $1\sigma$  noise level is  $\sim 0.004 \text{ K degree}$  for the longitude interval of  $0.03$ . (c) Galactic longitude-velocity diagram integrated over the latitude range from  $0.81$  to  $0.84$ . The dashed lines represent the radio-recombination-line velocity ( $-77 \text{ km s}^{-1}$ ) from Caswell and Haynes (1987). The spatial and velocity resolution are smoothed to  $52''$  and  $0.18 \text{ km s}^{-1}$ , respectively. The  $1\sigma$  noise level is  $\sim 0.004 \text{ K degree}$  for the latitude interval of  $0.03$ .

2つの分子雲は3 Myrに衝突し、O型星形成を引き起こし、孤立したBubbleができた、と仮説を立てる

衝突シナリオは2つの分子雲の形状、孤立したO型星の起源を説明できる

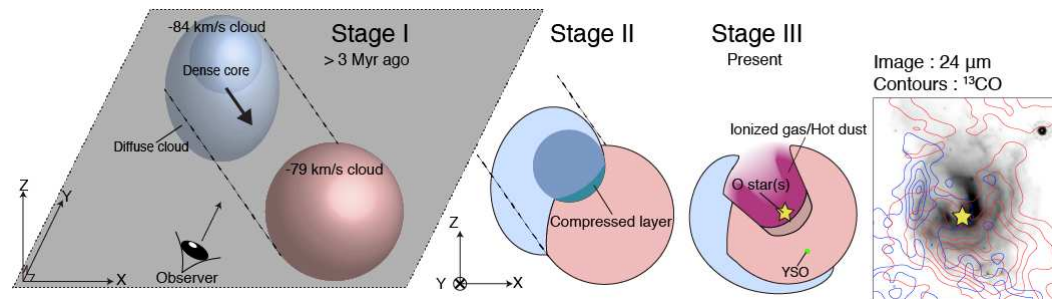


**Fig. 12.** Schematic image of a cloud-cloud collision scenario based on Habe & Ohta (1992) and Torii et al. (2015, 2017a). Stage I : a 3D image of the initial condition of the two clouds. Stage II : a 2D image of the two clouds in the X-Z plane at the time when the two clouds collide with each other. Stage III : a 2D image of the bubble in the X-Z plane. The Y-axis corresponds to the line of sight. The final panel shows the observational result for the two clouds superposed on the  $24 \mu\text{m}$  image.

# High spectral resolution observations toward Orion BN at 6 $\mu\text{m}$ : no evidence for hot water.

Nick Indriolo<sup>1</sup>, Jonathan C. Tan<sup>2,3</sup>, A. C. A. Boogert<sup>4</sup>, C. N. DeWitt<sup>5</sup>, E. J. Montiel<sup>6</sup>, D. A. Neufeld<sup>7</sup> and M. J. Richter<sup>6</sup>

天体：Orion BN

観測：6.7  $\mu\text{m}$ , 6.1  $\mu\text{m}$ , 5.7  $\mu\text{m}$ 。SOFIAに積まれたEchelon-Cross-Echelle Spectrograph (EXES)

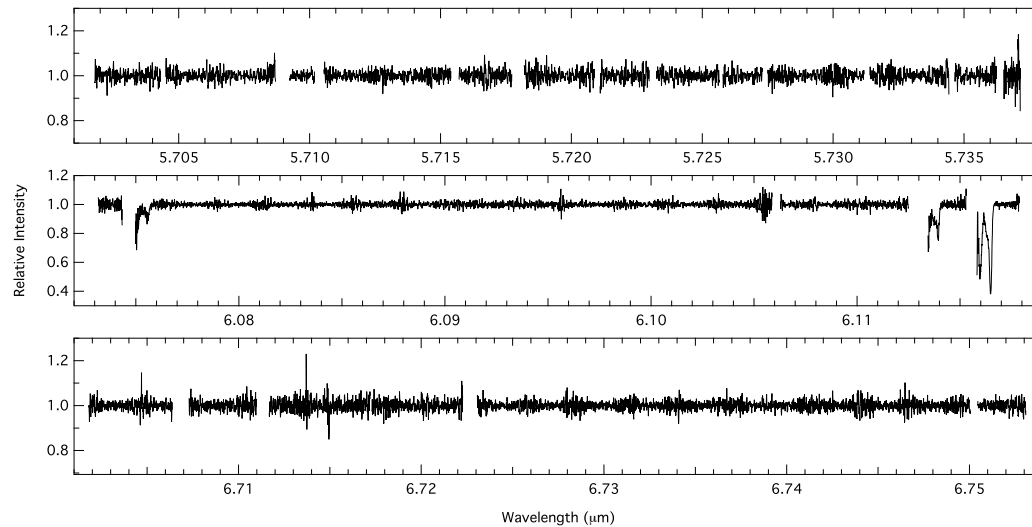


**Figure 1.** Spectra of Orion BN over the full wavelength range covered by our SOFIA/EXES observations. Each spectrum corresponds to a separate observation at a different grating setting. Oscillations in the noise level result from the cross-dispersed nature of the instrument, with higher noise regions coming from the edges of the individual echelle orders. Gaps in the spectra correspond to regions where telluric water vapor lines reduce transmission levels to near zero. The water absorption lines discussed herein are all from the spectrum in the middle panel.

手前の冷たい ( $\sim 70$  K) 高密度分子雲で  
で起こる $\text{H}_2\text{O}$ からの吸収を検出

水とCOの存在比  $N(\text{H}_2\text{O})/N(\text{CO})=5\times 10^{-3}$ 、  
水蒸気と氷の存在比

$N(\text{H}_2\text{O})/N(\text{H}_2\text{O}_{\text{ice}})\sim 0.04$  solid form

=> PDR環境を示す（薄い光脱離層中で、  
ice mantleから $\text{H}_2\text{O}$ が放出される）

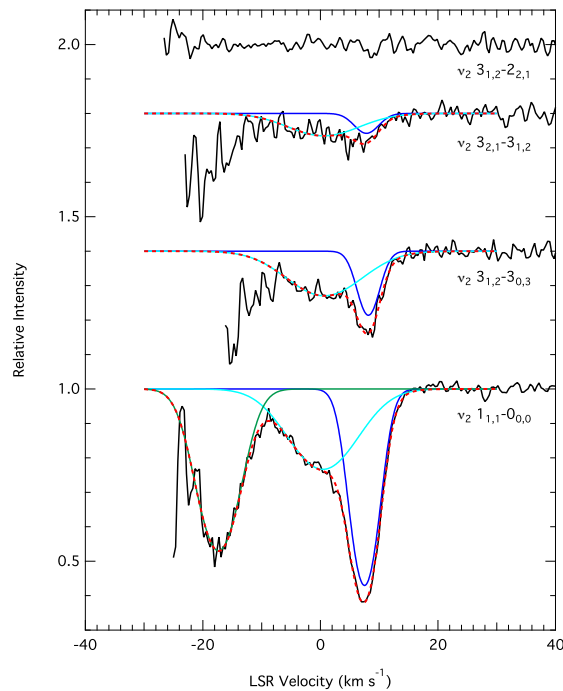


**Figure 2.** Spectra showing the water absorption lines observed toward Orion BN. Fits to the components at 8 km s<sup>-1</sup>, 0.5 km s<sup>-1</sup>, and -17 km s<sup>-1</sup>, are shown by blue, cyan, and green curves, respectively, and the sum of all components is shown as a red, dashed curve. The top spectrum shows a non-detection of the transition predicted to have the strongest absorption after the detected transitions in the observed wavelength range ( $\nu_2$  3<sub>1,2</sub>-2<sub>2,1</sub> at 6.1068262  $\mu$ m). Spectra have been shifted vertically for clarity.

**Table 1.** Absorption Line Parameters

Transition	Wavelength ( $\mu$ m)	$E_l/k_b$ (K)	$v_{\text{LSR}}$ (km s <sup>-1</sup> )	FWHM (km s <sup>-1</sup> )	$\tau_0$	$\int \tau dv$ (km s <sup>-1</sup> )	$N_l$ (10 <sup>15</sup> cm <sup>-2</sup> )
1 <sub>1,1</sub> -0 <sub>0,0</sub>	6.116331	0	7.5	5.3±0.2	0.84±0.02	4.78±0.19	2.35±0.09
3 <sub>1,2</sub> -3 <sub>0,3</sub>	6.113771	196.8	8.2	4.3±0.3	0.21±0.01	0.95±0.10	1.67±0.17
3 <sub>2,1</sub> -3 <sub>1,2</sub>	6.075447	249.4	7.8	4.8±0.4	0.06±0.01	0.31±0.05	0.51±0.08
1 <sub>1,1</sub> -0 <sub>0,0</sub>	6.116331	0	0.4	13.3±0.8	0.27±0.01	3.76±0.25	1.85±0.12
3 <sub>1,2</sub> -3 <sub>0,3</sub>	6.113771	196.8	0.7	14.7±1.1	0.13±0.01	2.17±0.19	3.82±0.33
3 <sub>2,1</sub> -3 <sub>1,2</sub>	6.075447	249.4	0.6	14.0±1.3	0.07±0.01	1.00±0.11	1.67±0.20
1 <sub>1,1</sub> -0 <sub>0,0</sub>	6.116331	0	-17	8.0±0.2	0.63±0.01	5.42±0.16	2.66±0.08

NOTE—Transition properties, parameters for the gaussian fits shown in Figure 2, and derived column densities.

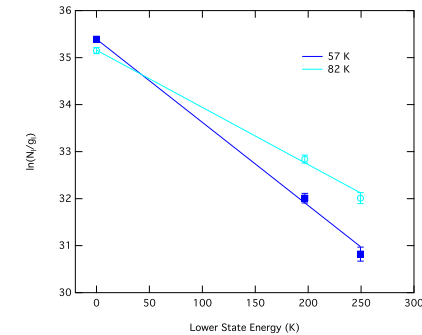


**Figure 3.** Rotation diagrams for the 8 km s<sup>-1</sup> component (blue) and 0.5 km s<sup>-1</sup> component (cyan). Color coding corresponds to the gaussian fits shown in Figure 2.

H<sub>2</sub>Oの吸収も放射も、BNの系速度では検出されず

BNの近傍でのH<sub>2</sub>Oの非検出は、現在の状況に新たな情報を与える => 力学的放出モデル？

例えば、BNがejection直前のprotostellar phaseにあったとすると、

高密度ガスの全てが剥ぎ取られたor星へ降着？

一方、Source IはmassiveなKeplerian降着円盤を持っている（Hirota et al. 2014; Ginsburg et al. 2018）

Orion分子雲中の冷たい高密度ガスによる近赤波長域での分子吸収の研究への役立つ？

天球面での分子雲構造の研究も徐々に可能になるかも。BNが速い固有運動を持っているので異なる時期での視線方向に沿って観測される手前のガスが変わる。



## Multiple star systems in the Orion nebula

**GRAVITY collaboration: Martina Karl<sup>1</sup>, Oliver Pfuhl<sup>1</sup>, Frank Eisenhauer<sup>1</sup>, Reinhard Genzel<sup>1,2</sup>,**

This work presents an interferometric study of the massive-binary fraction in the Orion Trapezium Cluster with the recently commissioned GRAVITY instrument. We observe a total of 16 stars of mainly OB spectral type. We find three previously unknown companions for  $\theta^1$  Ori B,  $\theta^2$  Ori B, and  $\theta^2$  Ori C. We determine a separation for the previously suspected companion of NU Ori. We confirm four companions for  $\theta^1$  Ori A,  $\theta^1$  Ori C,  $\theta^1$  Ori D, and  $\theta^2$  Ori A, all with substantially improved astrometry and photometric mass estimates. We refine the orbit of the eccentric high-mass binary  $\theta^1$  Ori C and we are able to derive a new orbit for  $\theta^1$  Ori D. We find a system mass of  $21.7 M_{\odot}$  and a period of 53 days. Together with other previously detected companions seen in spectroscopy or direct imaging, eleven of the 16 high-mass stars are multiple systems. We obtain a total number of 22 companions with separations up to 600 AU. The companion fraction of the early B and O stars in our sample is about 2, significantly higher than in earlier studies of mostly OB associations. The separation distribution hints towards a bimodality. Such a bimodality has been previously found in A stars, but rarely in OB binaries, which up to this point have been assumed to be mostly compact with a tail of wider companions. We also do not find a substantial population of equal-mass binaries. The observed distribution of mass ratios declines steeply with mass, and like the direct star counts, indicates that our companions follow a standard power law initial mass function. Again, this is in contrast to earlier findings of flat mass ratio distributions in OB associations. We exclude collision as a dominant formation mechanism but find no clear preference for core accretion or competitive accretion.

Accepted by A&A

<http://arxiv.org/pdf/1809.10376>

## VISION - Vienna survey in Orion. III. Young stellar objects in Orion A

**Josefa E. Großschedl<sup>1</sup>, João Alves<sup>1</sup>, Paula S. Teixeira<sup>1,2,3</sup>, Hervé Bouy<sup>4</sup>, Jan Forbrich<sup>1,5,6</sup>, Charles J. Lada<sup>6</sup>, Stefan Meingast<sup>1</sup>, Álvaro Hacar<sup>1,7</sup>, Joana Ascenso<sup>8</sup>, Christine Acker<sup>1</sup>, Birgit Hasenberger<sup>1</sup>, Rainer Köhler<sup>1</sup>, Karolina Kubiak<sup>1</sup>, Irati Larreina<sup>1</sup>, Lorenz Linhardt<sup>9</sup>, Marco Lombardi<sup>10</sup>, Torsten Möller<sup>9</sup>**

We extend and refine the existing young stellar object (YSO) catalogs for the Orion A molecular cloud, the closest massive star-forming region to Earth. This updated catalog is driven by the large spatial coverage ( $18.3 \text{ deg}^2$ ,  $\sim 950 \text{ pc}^2$ ), seeing limited resolution ( $\sim 0.7''$ ), and sensitivity ( $K_s < 19 \text{ mag}$ ) of the ESO-VISTA near-infrared survey of the Orion A cloud (VISION). Combined with archival mid- to far-infrared data, the VISTA data allow for a refined and more robust source selection. We estimate that among previously known protostars and pre-main-sequence stars with disks, source contamination levels (false positives) are at least  $\sim 7\%$  and  $\sim 2.5\%$  respectively, mostly due to background galaxies and nebulosities. We identify 274 new YSO candidates using VISTA/*Spitzer* based selections within previously analyzed regions, and VISTA/*WISE* based selections to add sources in the surroundings, beyond previously analyzed regions. The *WISE* selection method recovers about 59% of the known YSOs in Orion A's low-mass star-forming part L1641, which shows what can be achieved by the all-sky *WISE* survey in combination with deep near-infrared data in regions without the influence of massive stars. The new catalog contains 2978 YSOs, which were classified based on the de-reddened mid-infrared spectral index into 188 protostars, 184 flat-spectrum sources, and 2606 pre-main-sequence stars with circumstellar disks. We find a statistically significant difference in the spatial distribution of the three evolutionary classes with respect to regions of high dust column-density, confirming that flat-spectrum sources are at a younger evolutionary phase compared to Class IIs, and are not a sub-sample seen at particular viewing angles.

Accepted by Astronomy & Astrophysics

<https://arxiv.org/pdf/1810.00878>



## H<sub>2</sub>CO ortho-to-para ratio in the protoplanetary disk HD 163296

V.V. Guzmán<sup>1</sup>, K.I. Öberg<sup>2</sup>, J. Carpenter<sup>1</sup>, R. Le Gal<sup>2</sup>, C. Qi<sup>2</sup>, and J. Pagues<sup>2</sup>

<sup>1</sup> Joint ALMA Observatory (JAO), Alonso de Córdova 3107 Vitacura, Santiago de Chile, Chile; <sup>2</sup> Harvard-Smithsonian Center for Astrophysics, 60 Garden Street, Cambridge, MA 02138, USA

E-mail contact: viviana.guzman *at* alma.cl

Ortho-to-para (o/p) ratios of species like water, ammonia and formaldehyde (H<sub>2</sub>CO) are believed to encode information about the formation history of the molecule. Measurements of o/p ratios in protoplanetary disks could thus be used to constrain their physical and chemical histories. We present the first measurement of the H<sub>2</sub>CO o/p ratio in a protoplanetary disk, using three ortho and two para lines observed with the Sub-millimeter Array (SMA) combined with one highly resolved measurement of a single H<sub>2</sub>CO line with ALMA toward the disk around Herbig Ae star HD 163296. We find a disk-averaged H<sub>2</sub>CO o/p ratio of 1.8–2.8 (depending on the assumed disk structure), corresponding to a spin temperature of 11–22 K. We also derive a rotational temperature of 24 K from the flux ratio of the three ortho lines. The observed spatial distribution, as seen by ALMA, as well as the rotational temperature and the o/p ratio, at the large scales the SMA is most sensitive to, are consistent with a low-temperature formation pathway, most likely grain surface chemistry, of H<sub>2</sub>CO in this disk.

Accepted by ApJ

<http://arxiv.org/pdf/1809.01705>

## Capture and Escape: The Dependence of Radiation Forces on Clumping in Dusty Envelopes

Peter H. Jumper<sup>1</sup> and Christopher D. Matzner<sup>1</sup>

<sup>1</sup> Department of Astronomy and Astrophysics, University of Toronto, 50 St. George Street, Toronto, Ontario, M5S 3H4, Canada

E-mail contact: jumper *at* astro.utoronto.ca

Dust barriers effectively capture the photon momentum of a central light source, but low-density channels, along with re-emission at longer wavelengths, enhance its escape. We use Monte Carlo simulations to study the effects of inhomogeneity on radiation forces imparted to a dust envelope around a central star. We survey the strength and scale of an inhomogeneous perturbation field, as well as the optical depth of its spherical reference state. We run at moderate numerical resolution, relying on our previous resolution study for calibration of the associated error. We find that inhomogeneities matter most when their scale exceeds the characteristic mean free path. As expected, they tend to reduce the net radiation force and extend its range; however, there is significant variance among realizations. Within our models, force integrals correlate with the emergent spectral energy distribution, given a specified set of dust properties. A critical issue is the choice of integral measures of the radiation force: for strong deviations from spherical symmetry the relevant measures assess radial forces relative to the cloud centre of mass. Of these, we find the virial term due to radiation to be the least stochastic of several integral measures in the presence of inhomogeneities.

Accepted by MNRAS

<https://arxiv.org/pdf/1806.05686.pdf>

# First hydrodynamics simulations of radiation forces and photoionization feedback in massive star formation

Rolf Kuiper<sup>1</sup> and Takashi Hosokawa<sup>2</sup>

*Aims:* We present the first simulations of the formation and feedback of massive stars which account for radiation forces as well as photoionization feedback (along with protostellar outflows). In two different accretion scenarios modeled, we determine the relative strength of these feedback components and derive the size of the reservoir from which the forming stars gained their masses.

*Method:* We performed direct hydrodynamics simulations of the gravitational collapse of high-density mass reservoirs toward the formation of massive stars including self-gravity, stellar evolution, protostellar outflows, continuum radiation transport, photoionization, and the potential impact of ram pressure from large-scale gravitational infall. For direct comparison, we executed these simulations with and without the individual feedback components.

*Results:* Protostellar outflows alone limit the stellar mass growth only in an accretion scenario with a finite mass reservoir; when including accretion and ram pressure from large scales ( $> 0.1$  pc), protostellar outflows do not limit stellar mass growth at all. Photoionization and HII regions dominate the feedback ladder only at later times, after the star has already contracted down to the zero-age main sequence, and only on large scales. Specifically, photoionization yields a broadening of the bipolar outflow cavities and a reduction of the gravitational infall momentum by about 50%, but does not limit the stellar mass accretion. On the other hand, we find radiation forces restrain the gravitational infall toward the circumstellar disk, impact the gravito-centrifugal equilibrium at the outer edge of the disk, and eventually shut down stellar accretion completely. The most massive star formed in the simulations accreted  $95 M_{\odot}$  before disk destruction; this mass was drawn-in from an accretion reservoir of  $\approx 240 M_{\odot}$  and  $\approx 0.24$  pc in radius.

*Conclusion:* In the regime of very massive stars, the final mass of these stars is controlled by their own radiation force feedback.

Accepted by A&A

<http://adsabs.harvard.edu/pdf/2018A%26A...616A.101K>

<http://arxiv.org/pdf/1804.10211>